“Angular resolution expected from iCHORD orientation maps through a revisited ion channeling model”

Cyril Langlois, T. Douillard, S. Dubail, C. Lafond, S. Cazottes, J. Silvent, A. Delobbe, P. Steyer

“Angular resolution expected from iCHORD orientation maps through a revisited ion channeling model”

C. Langlois[1], T. Douillard[1], S. Dubail[2], C. Lafond[1], S. Cazottes[1], J. Silvent[3], A. Delobbe[3], P. Steyer[1]

[1]Université de Lyon, INSA-Lyon, MATEIS CNRS UMR5510, 7 avenue Jean Capelle, 69621 Villeurbanne (France)

[2]Axon Square SAS, 4 la Tuilière, 74140 Sciez (France)

[3]Orsay Physics, 95 Avenue des Monts Auréliens, 13710 Fuveau (France)

Abstract: Crystalline orientation maps are obtained in a Focused Ion Beam (FIB) microscope using the ion CHanneling ORientation Determination (iCHORD) method, which relies on the channeling phenomenon observed in ion-induced secondary electron images. The current paper focuses on the angular resolution that can be expected from such orientation maps, obtained using a revisited ion channeling model. A specific procedure was developed to evaluate the angular resolution, based on the distribution of orientation errors when evaluating controlled sample disorientation. The main advantage is that no external reference is required. An angular resolution of 0.9° is obtained on a nickel based sample using standard acquisition conditions. This value fulfills most of the needs in terms of microstructural characterization usually carried out by Electron Back Scattered Diffraction.

1. Introduction

Orientation mapping in a Scanning Electron Microscope (SEM) is now a common technique in academic and R&D laboratories through the Electron Back Scattered Diffraction (EBSD) technique. Useful information about crystallographic texture, strain localization and phase discrimination in samples of different natures (ceramics, metals, semiconductors, geological samples) are accessible. The requirements in terms of spatial resolution, angular resolution, and acquisition speed usually depend on the type of issue to be addressed. For local texture studies, statistical data are needed on a large number of grains, which means a high acquisition speed, whereas the angular resolution has not to be better than ~1°. A fast acquisition will also be necessary when covering a large area of a sample, which is particularly true for geological samples [1], or during *in situ* tests [2] and 3D acquisitions [3]. On the contrary, local strain characterization requires very high angular and spatial resolutions [4]. In this context, it is interesting to propose appropriate approaches to address these different materials science topics. For the EBSD technique, recent models of camera allow for either

high speed or high quality Kikuchi pattern acquisitions [5]. Apart from the camera, other acquisition configurations inside the microscope are proposed like off- or on-axis Transmission Kikuchi Diffraction (TKD) [6,7], which is adapted for thin samples in transmission mode and gives a better spatial resolution.

The Kikuchi diffraction is not the only way to obtain orientation maps on a polycrystalline bulk sample. The channeling contrast visible on images acquired using an ion beam in a Focused Ion Beam (FIB) microscope also contains crystallographic information that can be used to map the orientations without using an extra detector or a dedicated camera. The proof-of-concept and the *modus operandi* of this new method, called iCHORD for ion CHanneling ORientation Determination, is described in Langlois *et al.* [8]. Beyond the proof-of-concept, it is now crucial to determine the performance of iCHORD in terms of angular and spatial resolutions as well as acquisition/indexation speed in order to define potential targeted applications. In this work, the latests developments regarding the ion channeling model used in iCHORD are first exposed because it consists in the core of the iCHORD approach. The question of angular resolution measurement is then discussed and an original methodology suitable for iCHORD is proposed and applied on a standard iCHORD experiment.

2. Experimental details

All the experiments reported in this paper were carried out on a ZEISS NVision40 FIB-SEM instrument in order to obtain both ion-induced secondary electron images and EBSD orientation maps. The EBSD maps have been acquired with an Oxford Instruments™ F+ EBSD system (fast camera NordlysII and Channel 5 software). Concerning the ion source, the microscope is equipped with a SIINT Zeta column and a Ga liquid metal ion source (Seiko Instruments Inc. NanoTechnology, Japan). A sample tilt of 40° was systematically chosen. Actually, the tilt value must be high enough to allow the ion beam crossing several crystallographic planes, as explained in Langlois et al. [8]. Considering the chosen sample tilt and magnification, no dynamic focus was necessary. Conditions used for ion-induced secondary electron imaging on a texture-free copper sample were: 30 kV, beam current of 700 pA, pixel size of 110 nm and a dwell time of 120 ns. A series of 180 images (dimension 2048 x 1536 ; angular step 2°) was acquired in ~40 min resulting in an orientation map of dimension 1324 x 1372 pixels with a field of view of 145 µm. This set of data was used to illustrate the ion channeling model presented Section 3.

To determine quantitatively the angular resolution, a texture-free nickel alloy sample (Inconel 718) was used. Acceleration voltage and probe current were respectively equal to 30 kV and 1.5 nA, with a magnification of 600x, which corresponds to a pixel size of 93 nm. A complete rotation of 360°

was carried out in 60 min using an angular step of 2°. For each rotation step, two images were acquired, one with a dwell time of 1.6 µs per pixel, and a second one with a shorter dwell time equal to 0.12 µs. All the images with a dwell time of 1.6 µs constitute the image series #1 whereas all the images acquired with a dwell time of 0.12 µs constitute the image series #2. Raw image dimensions are 2048 x 1536 pixels, corresponding to a field of view of width 190 µm. After mutual image alignment, the two image series are reduced to dimensions 1320 x 1224 pixels (field of view of width 123 µm), mainly due to the fact that the scan rotation is not corrected during the sample rotation. For all the calculations related to the angular resolution determination exposed in Section 5, six-binned versions (without averaging) of the two Inconel image series were used to limit the computation time.

For the acquisition of these different images series, ion currents up to 1.5 nA were used considering the good resistance of copper and nickel toward ion sputtering.

3. Modeling the ion channeling

To compute a theoretical intensity profile for a given orientation of the crystal, Langlois *et al.* [8] have used a model based on crystallographic calculations involving a lot of parameters to be manually set to properly fit the experimental intensity profiles. In the present work, a more numerical approach is used, based literally on the principle of "ballistic channeling" of incident particles. To date, this approach has been tested only for cubic structures, and the adaptation for other crystallographic systems is in progress.

Atomic positions are first generated for the cubic crystal of interest in the form of an array A containing atom coordinates as well as atom type. For most cases, a volume of 6 x 6 x 6 unit cells is enough for the calculations, centered on the origin of the coordinates frame. At the beginning of the modelization process, the crystal axes are aligned with the orthonormal reference frame of the microscope with the ion beam parallel to $\vec{e}_z$. Since we want to compute a theoretical intensity profile for a crystal with an orientation defined by its three Euler angles $(\varphi_1, \phi, \varphi_2)$ in the Bunge's convention, the atomic positions are first rotated according to the active orientation matrix M defined by [9]:

$$M = \begin{pmatrix} \cos\varphi_2 \cdot \cos\varphi_1 - \sin\varphi_2 \cdot \cos\phi \cdot \sin\varphi_1 & -\cos\varphi_2 \cdot \sin\varphi_1 - \sin\varphi_2 \cdot \cos\phi \cdot \cos\varphi_1 & \sin\varphi_2 \cdot \sin\phi \\ \sin\varphi_2 \cdot \cos\varphi_1 + \cos\varphi_2 \cdot \cos\phi \cdot \sin\varphi_1 & -\sin\varphi_2 \cdot \sin\varphi_1 + \cos\varphi_2 \cdot \cos\phi \cdot \cos\varphi_1 & -\cos\varphi_2 \cdot \sin\phi \\ \sin\phi \cdot \sin\varphi_1 & \sin\phi \cdot \cos\varphi_1 & \cos\phi \end{pmatrix}$$

Euler angles $(\varphi_1, \phi, \varphi_2)$ represent the orientation of the crystal that would be found in an EBSD map. A new array A' now contains the updated atomic positions A'_i given by:

$$A'_i = M \cdot A_i$$

defined in the microscope reference frame. In the iCHORD acquisition setup (see Figure 1. of Langlois *et al.* [8]), the sample is tilted around the $\vec{e}_x$ axis at a constant angle of $\psi = 40°$, and rotated around the tilted rotation axis with an angular step $\Delta\theta$ until a complete turn is achieved, which means $N = (360 / \Delta\theta)$ rotations. It is then necessary to compute the array A'' containing the atomic positions for a given rotation step, in order to calculate the corresponding intensity level.

3.1. Orientation matrix of the crystal during the acquisition procedure

At the beginning of the acquisition process, the direction perpendicular to the sample surface is along $\vec{e}_z$. The initial operation is a tilt around $\vec{e}_x$ at a constant angle of $\psi = 40°$. The corresponding active rotation matrix is given by:

$$T_\psi = \begin{pmatrix} 1 & 0 & 0 \\ 0 & \cos\psi & -\sin\psi \\ 0 & \sin\psi & \cos\psi \end{pmatrix}$$

Then, the sample is rotated around its tilted surface normal direction. For each rotation step, the atomic positions are left-multiplied by an active matrix $R_{\Delta\theta}$ corresponding to a rotation of $\Delta\theta$ around the tilted rotation axis $\vec{t} = T_\psi \cdot \vec{e}_z = \begin{vmatrix} 0 \\ -\sin\psi \\ \cos\psi \end{vmatrix}$. The matrix $R_{\Delta\theta}$ is defined using the formulae that yields the active rotation matrix corresponding to the axis-angle pair $(\vec{t}, \Delta\theta)$ [9]:

$$R_{\Delta\theta} = \begin{pmatrix} \cos\Delta\theta & -\cos\psi\cdot\sin\Delta\theta & -\sin\psi\cdot\sin\Delta\theta \\ \cos\psi\cdot\sin\Delta\theta & \cos\Delta\theta + \sin^2\psi\,(1-\cos\Delta\theta) & -\sin\psi\cdot\cos\psi\,(1-\cos\Delta\theta) \\ \sin\psi\cdot\sin\Delta\theta & -\sin\psi\cdot\cos\psi\,(1-\cos\Delta\theta) & \cos\Delta\theta + \cos^2\psi\,(1-\cos\Delta\theta) \end{pmatrix}$$

After p rotation steps, the atomic positions A''_i stored in array A'' are obtained by:

$$A''_i = (R_{\Delta\theta})^p \cdot T_{\psi=40°} \cdot A'_i$$

Once the atomic positions are computed for this rotation state, the question becomes: how to determine the intensity received by the detector?

3.2. Intensity simulation

According to the ballistic description of the channeling effect [10], if interplanar spaces are available for the ion beam to travel in, the intensity will be low because the secondary electron emission will be generated too deep under the surface, so that most of electrons do not reach the surface and then the detector. To simulate this effect, an algorithm has been developed, fully detailed in Appendix A and briefly described hereafter to clarify several choices made to avoid simulation artefacts. To compute the intensity value at a given rotation state, atomic positions contained in array A'' are projected onto a plane perpendicular to the ion beam (so, perpendicular to $\vec{e}_z$). To avoid projection artefacts, only the atomic positions contained in a sphere of radius equal to 3 unit cells and centered on the origin are projected. The choice of a sphere is justified by less projection artifacts: the area on which the atoms are projected is constant for all orientations and rotation steps, which is not the case if the full 6 x 6 x 6 unit cells parallelepiped is projected. Atoms have their respective atomic radius and they project themselves orthogonally as discs in the projection plane, which is tangent to the sphere. To take into account the decreasing interactions between the ion beam and the atom as a function of the depth, a brightness value in the range 0-255 is associated to each atom (and each discs in the projection plane) following a decreasing function of type $G(d) = a \cdot d^b$ (see Figure 1a and 1b) with d the distance between the atom and the projection plane. When parts of discs overlap on the projection plane, the part which belongs to the atom with the smallest distance to the projection plane has the priority to give its brightness in the projection. An example of such projection is presented in Figure 1b.

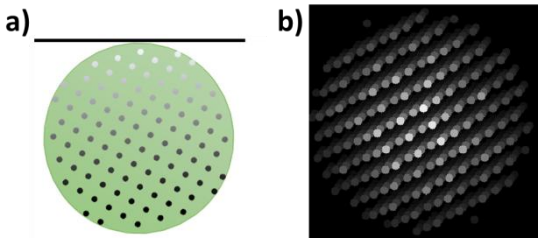

Figure 1. *Computation of the intensity in a given orientation during the rotation series acquisition. a) Atomic brightness as a function of the distance toward the projection plane represented by the black line on the top; b) Projection plane on which atoms are projected in the form of disks of different brightness levels.*

After the projection, let us consider now the sum of the brightness values s_i for all the pixels i constituting the projection plane:

$$S = \sum_i s_i$$

In the projection plane, the channeling condition corresponds to low values for S because, for instance in the extreme case of a low index zone axis, a complete row of atoms will project itself onto one single disc, leaving a large area with brightness levels equal to zero. On the contrary, in non-channeling conditions, most of the pixels of the projection plane will have non-zero brightness levels, resulting in high values for S . Due to this strong correlation, the value S is associated to the theoretical intensity value for this rotation step. A complete intensity profile is obtained by repeating the intensity calculation for each rotation step. At the end of the process, if it helps to obtain a better fit with the experimental intensity profiles, the theoretical intensity profiles are raised to a power between 1 and 5. All the theoretical and experimental profiles are normalized by dividing each value of a profile by its norm.

3.3. Adjustment of the parameters

As already mentioned, a sphere radius equals to 3 unit cells is enough to model the channeling effect in the projection plane. Other parameters to be adjusted in the simulation are the size of the projection in pixels, the atomic radii, the value of the decay factor 'a', value of decay power 'b' for the function $G(d)$ and the power on the output profile. For the size of the square projection area (in pixels), a default value limiting the calculation time while keeping reasonable fidelity compared to experimental values is 8 times the diameter of the sphere with a one-to-one correspondence between Angströms and pixels. For example, for copper with lattice parameter $a = 3.615$ angstroms, the diameter of the sphere is $D_{sphere} = 6 \cdot a$ so the square projection size will be $48 \cdot a = 175$ pixels. Atom radii can be chosen following different models (atomic-ionic radii [11] and crystal radii [12]) according to the structure studied, with eventually a scaling factor that applies on all radii. Standard parameters are: decay factor 'a' equal to 3, decay power 'b' equal to 4 and an output power equal to 2. After a first run with these standard parameters and a small database (i.e. 200k profiles), a coarse orientation is found, that is used to refine the parameters. Then, a complete database is computed. This work has to be done only once for each material and iCHORD acquisition configuration (tilt angle and high tension). Once the database is computed, it can be used for any experimental data acquired in the same conditions with the same materials.

3.4 *Application example on copper sample*

In order to evaluate the model, it is necessary to measure how close theoretical and experimental profiles are, for a representative set of known orientations. To achieve this comparison, an iCHORD acquisition has been performed on a polycrystalline copper sample without any marked texture (Figure 2a). An EBSD map was also acquired on the same area, in order to obtain the Euler angles at each position from which theoretical profiles can be computed (Figure 2b). The "distance" between experimental (E) and theoretical (T) profiles obtained at the same position is expressed with the following formula:

$$\text{distance} = 1 - E \cdot T$$

with profiles E and T considered as two vectors of same dimension to compute their dot product. Using this formula, two profiles are very close if their associated distance is close to zero. The distance map for each position of the region of interest is presented Figure 2c, together with the distribution of these distances (Figure 2d). The distances between the experimental and theoretical profiles are close to zero throughout the area, with a narrow distribution peaked at 0.005. It is obviously not the case at grain boundaries and positions corresponding to dust on the sample surface. It is worth mentioning that the sample is not textured, so that many random orientations are represented in the region of interest. It means that the developed model computes theoretical profiles with high fidelity whatever the orientation. These results have been confirmed on several other cubic materials such as TiN [8], Co and Ni superalloys [13], Al and Fe.

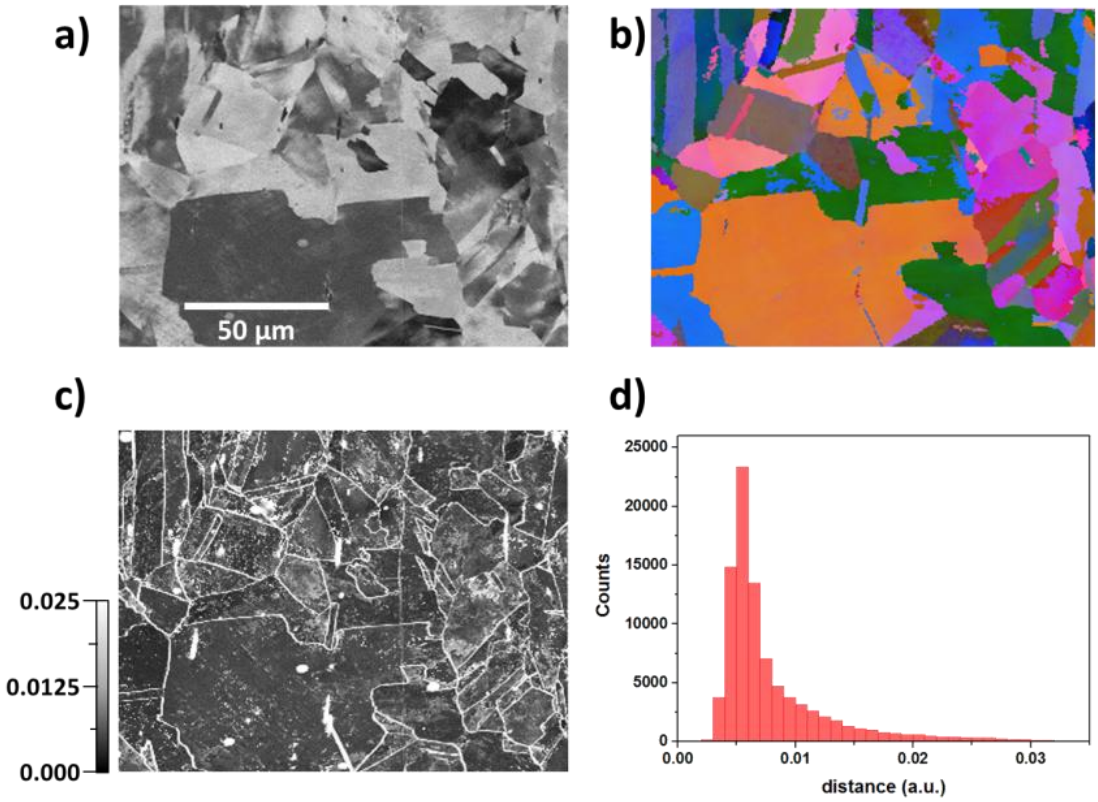

Figure 2. *Evaluation of the ion channeling model on a copper sample. a) image extracted from the ion image series, b) denoised EBSD Euler map on the same area aligned with the ion image series, c) map of the "distance" (see text for the definition of "distance" in this context) between experimental and theoretical profiles for each orientation in the region of interest, d) distribution of the 'distance' map values. White pixels on c) represent distances equal or superior to 0.025.*

To help the reader visualizing the agreement between theoretical and experimental profiles, Figure 3 gathers on the same plot theoretical and experimental profiles extracted from a position in the ion image series corresponding to Euler angles $\left(162.35^{\circ} \quad 28.94^{\circ} \quad 2.47^{\circ}\right)$. This position has been chosen because the distance between the two profiles is 0.0055, which is the peak value of the 'distance' distribution presented Figure 2d. It means that, globally, the agreement presented for this specific orientation is representative of the situation for other orientations.

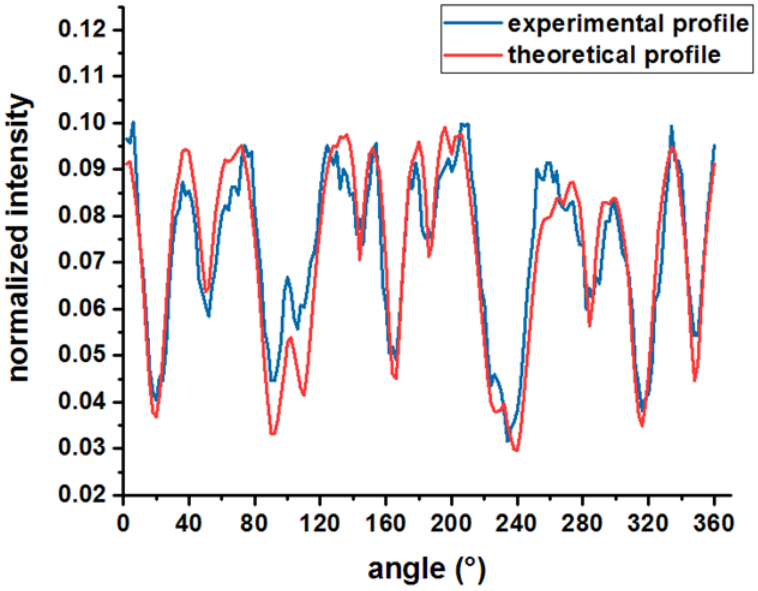

Figure 3. *Representative example of correspondence between experimental and theoretical profiles for the Euler triplet* $\left(162.35^{\circ} \quad 28.94^{\circ} \quad 2.47^{\circ}\right)$. *The distance between the two profiles is 0.005, which is the most frequent distance between experimental and theoretical profiles in the tested area on copper sample.*

4. Robustness of the revisited ion channeling model toward orientation indexation

4.1. Relationship between distance and disorientation for two theoretical profiles

The central question for orientation mapping is the ability to distinguish between two very close orientations from their signatures, which are their experimental profiles in the iCHORD approach. The signature differences must be related to the disorientation between these two close orientations. This relationship cannot be precisely evaluated experimentally because the orientations are initially not known. Using EBSD would be useless because of the different acquisition geometry leading to orientation errors and spatial distortions as well as the very large amount of experimental data that would be necessary to sample experimentally the orientation space. However, the analysis can be carried out at least theoretically, shedding light on the relationship between orientation and intensity profiles.

The first step of the analysis is to generate a set of 100 000 random orientations in the fundamental zone corresponding to the cubic system. For each orientation of this set, a theoretical profile (vector of 180 components) is computed using the model exposed in Section 3. Then, among this orientation set, 5 000 pairs of orientations are selected with the condition that their disorientation is under 3° because the focus is on the separation between close orientations. More

precisely, to construct such pairs, an orientation is selected with its theoretical profile, and a search of the best match is performed in the set of 100 000 profiles. Because the orientation set is small (100k orientations only), the disorientation corresponding to this match is distributed between 0° and 3°, which corresponds to the intended analysis. For more details concerning the construction and use of such random orientation set, see Appendix B.

Figure 4 shows a graph with disorientation as a function of the distance. Each pair (distance ; disorientation) previously computed is represented by a red data point. In order to illustrate the influence of the database size on the distance and disorientation ranges, the same analysis has been carried out using datasets of 250 000, 500 000 and 1 000 000 profiles, and results have been added also on Figure 4 (see the figure caption of associated colors).

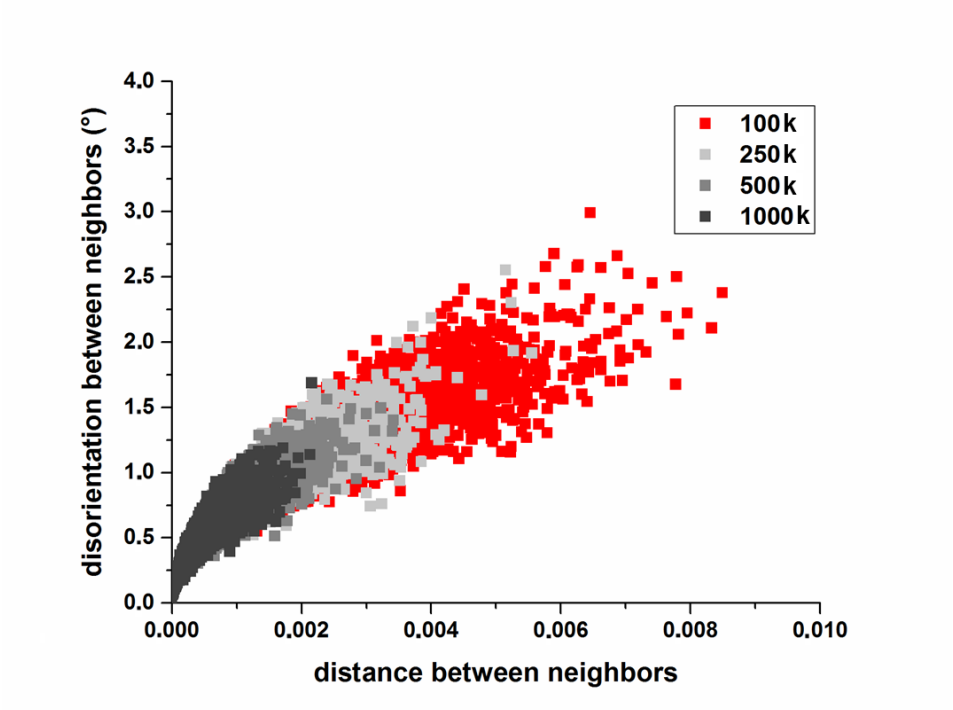

Figure 4. *Disorientation as a function of the distance for pairs of orientations. Results using different dataset sizes are presented.*

It appears that the relationship linking the distance between pairs and their disorientation is not linear. It is worth noting that for a given distance, the possible disorientation interval is bounded, and that this interval is converging toward low values when the distance decreases down to zero, which is the fundamental core of the indexing procedure, described in Appendix C. It can be concluded that the distance between profiles is a pertinent indicator of the disorientation for small distance values. However, one can expect slightly lower experimental performance compared to the results of this purely theoretical analysis. As an illustration, let us recall the results from Section 3.4 on copper sample, for which the distance between an experimental profile and a theoretical profile

of same orientation (at least the one given by EBSD) was distributed around the value 0.005. This quite large value compared to the theoretical analysis underlines that 1/ the channeling signal may be degraded by experimental factors (noise, image distortions), 2/ errors in image series alignment may also affect the effective profile on a given position, and 3/ the model itself has some limitations. These reasons limit the agreement between the experimental ion channeling and its modelization, resulting in larger distances between experimental and theoretical profiles. Hopefully, the disorientation interval is expected to stay quite narrow for such distance values, as it will be shown on Section 5.

4.2. Disorientation vs distance analysis with different profile dimensions

It is interesting to test whether the relationship between disorientation and distance is kept when decreasing the dimension of the profiles. If it is the case, less experimental images would be necessary to compute an orientation map. The same analysis has been carried out by reducing the theoretical profile dimension in the 100k dataset and the 5k dataset, with a renormalization of each profile. Dimensions 180, 90, 45 and 30 have been tested and the results are presented Figure 5.

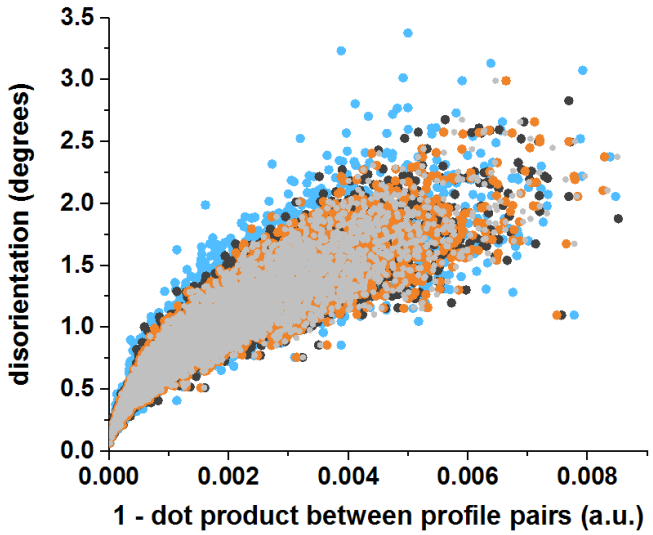

Figure 5. *Disorientation as a function of the distance for pairs of orientations for profile dimensions 180 (grey), 90 (orange), 45 (dark grey) and 30 (blue).*

It appears that the range of disorientation associated to a given distance increases when the dimension of the theoretical profiles is reduced. Accordingly, the capability to discriminate between close orientations is then degraded, especially when the distance is large. However, it is worth noting that the disorientation range associated for distances lower than 0.0075 does not strongly depend on the profile dimension. Experimentally, it means that, when working with small number of images (i.e.

small profile dimension), the size of the database must be increased to obtain smaller distances (see Appendix B) and keep the associated disorientation range as small as possible.

5. Evaluating the angular resolution

Different approaches may exist to evaluate the angular resolution associated to an iCHORD experiment carried out with given acquisition and post-treatment parameters. As the EBSD technique has proven to reach a very high angular resolution provided some precautions in the acquisition and data treatment, EBSD measurements could be used as a reference. However, the differences in scan system and acquisition geometry induce image distortions, and the identification of homologous points in the two maps is an issue [14]. Moreover, the quality of our EBSD acquisitions could be also questionable as our setup is designed for acquisition speed rather than angular resolution. Keeping in mind these restrictions, the comparison between EBSD and iCHORD measurements on the same area can be nevertheless interesting, and was carried out in previous studies on a TiN sample (proof-of-concept article [8]) and nickel superalloy by Vernier *et al.* [13]. The good agreement between EBSD and iCHORD maps for these two non-textured materials allows concluding that for any orientation, the probability of a large error in the orientation determination is small.

Considering EBSD measurements, it is a current practice to measure the orientation noise on a monocrystal to evaluate the angular precision of the measurements. This method is not really adaptable to a pattern matching technique like iCHORD because of its discrete nature. Results also depend on the orientation measured[15]. Another solution would be to measure a known misorientation between two points on the sample surface. This can be achieved by measuring the misorientation across a twin boundary in a cubic material. If the sample is free of any deformation, all the measurements are supposed to give a result of 60°, and any deviation from this value (*i.e*. a standard deviation calculated from many measurements) can be interpreted as the angular resolution of the technique. However, this evaluation of angular resolution requires a lot of measurements to be statistically reliable, and will not be considered here.

We propose in this study a method based on the measurement of a controlled disorientation. The successive steps of the method are exposed hereafter through a case study. First, two iCHORD orientation maps have been acquired on a nickel alloy (series #1 and #2 detailed in Section 2). These two acquisitions were realized one after the other and were aligned together. The next step consists in introducing a controlled disorientation between the two series by operating a cyclic image permutation in series #2, which results in an arbitrary disorientation of 6°. At this stage, all the intensity profiles extracted from the series #2 are supposed to be shifted by 6 degrees compared to

the ones of the first stack. Then, the profiles of the two series are indexed separately and a point-to-point disorientation between homologous positions is calculated. In the ideal case, the disorientation map is supposed to display a constant disorientation, and the statistic deviation from this constant disorientation can be interpreted as the angular resolution. In the present case, a value of 6 degrees has been chosen to display a deviation distribution away from 0° value, that can be fitted with a gaussian curve. A direct interpretation of the gaussian standard deviation in terms of angular resolution is then possible.

As mentioned in the experimental details section, the time per pixel has been reduced for the second series to avoid ion sputtering. Profiles extracted from series #2 then exhibit a lower signal-to-noise ratio. This may impact the evaluation of the angular resolution but is inherent to our method for evaluating the angular resolution. Results obtained with a database of 1000k profiles are presented in Figure 6. The first image of the initial stack is shown in Figure 6.a to illustrate the region of interest. Figures 6.b, 6.c and 6.e correspond respectively to the EBSD orientation map, the CHORD map computed from image series #1 and the CHORD map computed from 6°-disoriented image series #2. The disorientation maps “series #1 versus EBSD” and “series #2 versus series #1” are presented respectively in Figure 6.d and 6.f. The distributions of the disorientation values are presented on the same graph in Figure 6.g. On this graph, the disorientation distribution between series #1 and EBSD values was fitted with a log-normal curve (no negative values for disorientations) whereas values extracted from the second disorientation map are plotted as the disorientation deviation (positive and negative) from 6° and fitted with a gaussian function. The standard deviation of the latter is equal to 0.9°. Actually, this qualitative result must be refined: to evaluate the angular resolution, one has to verify to which extent the orientations obtained by indexing series #2 corresponds to what is expected, which is the series #1 set of orientations artificially rotated by an angle of 6° around $\vec{e}_z$. Results are presented in Figure 6.g, with a log-normal fit centered on 0.75°, with 80% of the values under 1° of disorientation. This statistical result allows concluding that the angular resolution can be reasonably considered to be better than 1°.

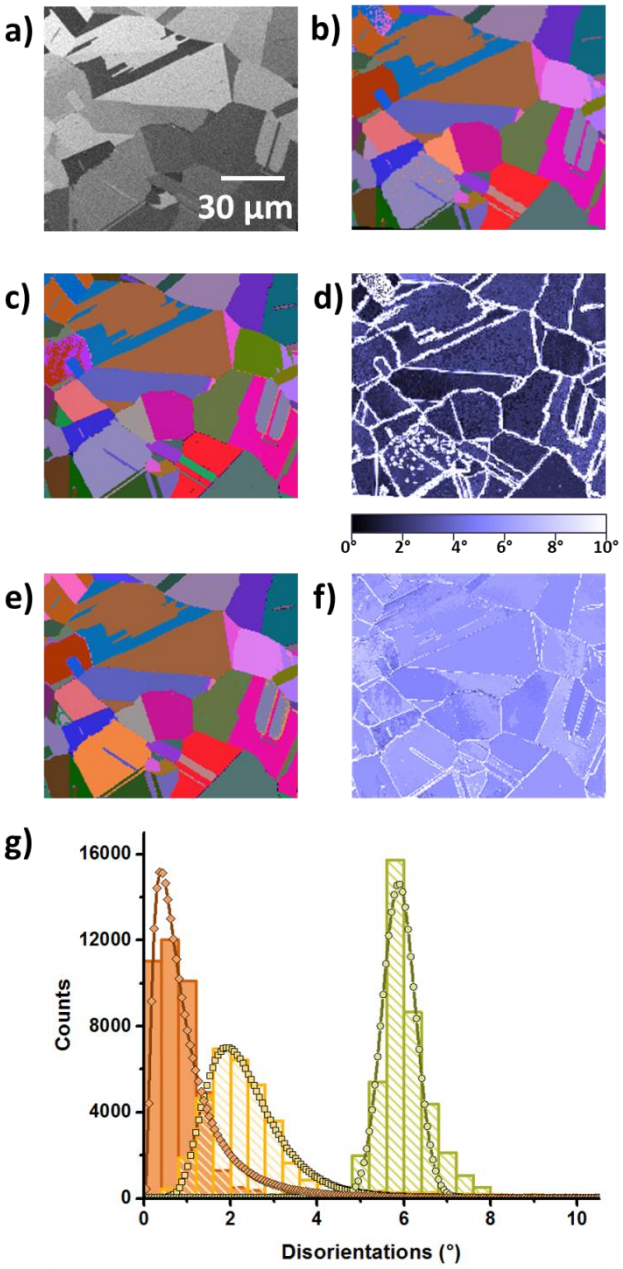

Figure 6. *Experimental evaluation of the angular resolution associated to iCHORD orientation mapping. a) first ion-induced secondary electron image of the image series #1, b) EBSD Euler map on the same region of interest aligned with image series #1, c) iCHORD Euler map computed from image series #1 with the same sample orientation as EBSD, d) disorientation map between iCHORD and EBSD orientations, e) iCHORD Euler map computed from image series #2 after a rotation of 6° compared to EBSD and image series #1, f) disorientation map between orientation values from iCHORD maps #1 and #2, g) distributions of disorientation values : in yellow (square symbols), disorientation map between iCHORD map #1 and EBSD measurements ; in green (circular symbols), disorientation map between iCHORD maps #1 and #2 ; in orange (losange symbols), disorientation between iCHORD map #2 and expected values computed from iCHORD map #1.*

Our strategy to evaluate the angular resolution is based on the measurement of a known disorientation. It is important to estimate the strengths and weaknesses of such approach. First, it is

worth mentioning that this method is applied directly on the area of interest. It allows evaluating the angular resolution associated to a given experiment, without referring to previous calibration experiments realized with different imaging conditions on different samples, with the question of time stability. However, it is not always possible to acquire a second image series on the same area if the material is beam sensitive. A way to circumvent this problem would be to create artificially the second series by duplicating series #1 and applying the cyclic image permutation. In this case, it does not probe the fidelity of the iCHORD method because only one measurement is carried out.

More generally, it should also be noted that this method characterizes only the iCHORD angular resolution when measuring rotations in the plane of the sample that results in a simple profile shift. It brings no proof that measuring disorientations along different orientation paths would not yield different angular resolution values. This argument is partially offset by mainly two reasons. Firstly, the indexing algorithm does not depend strongly on the orientation (see Section 4.1). It means that there is no difference of treatment when evaluating the disorientation between two profiles presenting a shift and two completely different profiles: if the distance is the same between the two profiles, the disorientation will stay in the interval associated to this distance (see Figure 4). Secondly, the iCHORD orientation measurements are in line with EBSD, as proven by Figure 6.d and 6.g (black distribution) and other published work relative to iCHORD [8,13]. It can be concluded that a systematic error in iCHORD measurements that would not appear in our angular resolution strategy is not likely.

The experiments presented in this study have been carried out in standard conditions and using the standard goniometer shipped with the microscope. The value of 1° can then be considered as the standard angular resolution of iCHORD at the present time. As emphasized in the introduction, this angular resolution depends on the experimental parameters and post-treatment conditions. Referring to Section 4.2, using a larger angular step during the acquisition (less images in the iCHORD image series) increases the disorientation range associated to a given matching score. As a consequence, a broader distribution with a larger standard deviation is expected for the angular resolution. It is then necessary to work with a larger database to partly compensate for this lack of information by obtaining lower distances between experimental and theoretical profiles when searching in the database.

6. Conclusion

A novel approach is proposed for simulating the channeling contrast observed in ion-induced secondary electron images. This approach involves less parameter compared to our previous work, is more versatile, and may readily take into account, in the future, crystals of any symmetry. An original

strategy for evaluating the angular resolution of iCHORD orientation maps is proposed, without referring to external measurements or reference. Adopting this new determination method of the angular resolution, an experimental value slightly below 1° has been found. If such angular resolution value is still high to be used for strain mapping, it is perfectly suitable for texture determination, *in-situ* and 3D mapping.

Appendix A. Projection algorithm for computing theoretical intensity profiles

The procedure mentioned in part 3.2 is applied according to the algorithm described in the present Appendix, starting from the array A'' containing the atomic position at a given rotation step.

- For each atom i with coordinates $(x_i\ y_i\ z_i)$ in A'', transfer its coordinates in a new array B if $x_i^2 + y_i^2 + z_i^2 \leq (3 \cdot a)^2$, a being the lattice parameter. This corresponds to the selection of atoms contained in a sphere of radius equal to $3 \cdot a$.
- For each atom i in B, compute the distances d_i between the atom and the projection plane. These distances are equal to $3a - z_i$.
- For each atom i in B, considered by ascending values of d_i, select and store in an associated list L_i all pixels j in the projection plane that respect the conditions $(x_j - x_i)^2 + (y_j - y_i)^2 \leq r_i$, r_i being the atomic radius selected for atom i.
    - For each pixel j in list L_i, if no grey level has been set previously, assign the grey level s_i given by the function $G(d_i) = a \cdot d_i^{\,b}$, a and b being user-defined parameters with standard values described in section 3.3.
- Store in an array P all pixels i of the projection plane with coordinates respecting the condition $|x_i| \leq 3a + r$ AND $|y_i| \leq 3a + r$, r being the largest atomic radius in the structure considered
- Compute the value $S = \sum_i s_i$ for all pixels i in P, s_i being the grey value of pixel i.

The value S corresponds to the intensity at the rotation angle for which the array A'' has been computed. For a complete intensity profile, the process must be repeated by computing the array A'' for the different rotation angles and following the above mentioned algorithm to extract the corresponding intensity value.

Appendix B. Stochastic sampling of cubic fundamental zone

The simplest way to sample the orientation space (SO3) [16] is to increment by a fixed step the three Euler angles, in a range defined from the symmetry of the phase considered. Many drawbacks are associated with this way of sampling the orientation space. For instance, for a cubic material and using the Bunge's notation, the first Euler angle φ_1 is usually incremented from 0° to 360° whereas the second and third ones (Φ and φ_2) range between 0° and 90°. In this sampling scheme, a single orientation is represented three times (rotation around a three-fold axis) [17]. Moreover, some parts of the orientation space are sampled more finely than others [18]. This is the reason why in such calculations, other sampling schemes and coordinate systems are currently used [19,20]. In the present study, a stochastic approach is used using quaternions, following Morawiec's book "Orientations and Rotations" [16]. A set of N random quaternions consists in a statistical sampling of the orientation space. A consequence of this stochastic method is that no fixed disorientation exists between two neighbors in the orientation space. On the contrary, these disorientations between neighbors form a peaked distribution. Figure A.1 presents such distributions for different sampling, i.e. 100k, 250k, 500k and 1000k orientations randomly created. Finer and finer sampling can be obtained by just adding chunks of orientations, each of them sampling sparsely the whole orientation space. In this way, it is quite easy to vary the size of the database.

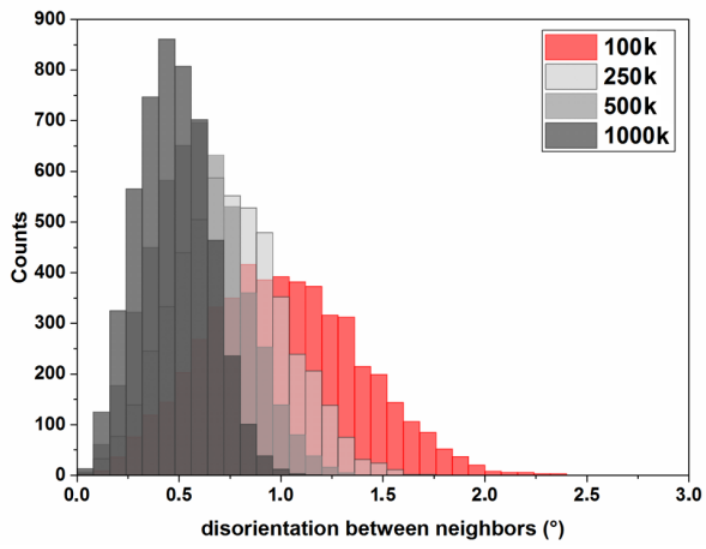

***Figure A.1**. Distributions of disorientations between neighbors in SO3 samplings of different sampling sizes.*

A convenient way of dealing with such distributions is the cumulative view, from which the percentage of values being below a threshold value can be easily extracted. For each distribution, the percentage of disorientations between neighbors below 1° and 1.5° are presented in Table A.1.

Number of orientations in the SO3 sampling	Probability to have a disorientation less than 1°	Probability to have a disorientation less than 1.5°
100k	54.7 %	90.6 %
250k	85.4 %	99.7 %
500k	97.2 %	100 %
1000k	99.9 %	100 %

Table A.1. *Percentages of disorientations between neighbors lower than 1° and 1.5° for different SO3 sampling sizes.*

Appendix C. Database search algorithm

Concerning the search algorithm for the profile indexation, it has been shown that "tree algorithms" are efficient and allow saving a lot of time compared to an exhaustive search [8]. However, in general, they are not suited for high dimension vectors as in our case. Actually, when it is possible, it is always better to use the specificities of a problem into the algorithm than implementing the algorithm "as is". As an application of this concept, a more robust route is proposed here, that takes into account the similarity between profiles of the same grain and globally inside the region of interest.

First, a list L of all experimental profiles is constituted and randomly sorted. Then, the following steps are carried out:

For each profile X of list L				
	If X has not been associated with a theoretical profile			
		Find the closest theoretical profile T compared to profile X with exhaustive search		
		Associate X to T and store the score R		
		For each profile X' of list L with no theoretical profile associated		
			Calculate R' = score between X' and T	
			Calculate V = score between X and X'	
			If (V<R) AND (R'<R)	
				Associate the theoretical profile T to X'
		END For		
	END If			
END For				

Table B.1. *Description of the similarity search algorithm.*

In this algorithm, the score corresponds to one minus the dot product between the two profiles. A score close to 0 indicates a short "distance" between the two profiles. This algorithm can

be easily parallelized on multiple processors provided a controlled access to the list L. Once all profiles X of L are associated with a theoretical profile (with the algorithm or by exhaustive search), it is possible to start a new cycle with a new list L' filled with experimental profiles that have been indexed without an exhaustive search, *i.e.* by similarity approach. This scheme allows very rapidly obtaining in a first cycle a complete orientation map of good quality. If more precision is required, the calculations can continue until having performed an exhaustive search on all the experimental profiles. In all the results presented in the present work, only one cycle has been carried out because the difference compared to a fully exhaustive search is negligible and the gain in indexation time is considerable. It depends of course of the degree of similarity of the profiles in the region of interest, which is closely linked to the number of grains in the region of interest. If a large number of grains are present, the number of profiles with a common orientation is low and the number of exhaustive searches will be higher. The proportion of grain boundaries also increases, which slows down the indexation rate because grains boundaries do not present any similarity. To sum up, depending on the number of grains in the region of interest, indexing with the similarity algorithm in one cycle can decrease by a factor 8 to 20 the indexing time compared to an exhaustive search carried out for each pixel. This concept could also be used in several other pattern matching issues, and particularly for the EBSD dictionary indexing [21].

References

[1] A. Ceccato, G. Pennacchioni, L. Menegon, M. Bestmann, Crystallographic control and texture inheritance during mylonitization of coarse grained quartz veins, Lithos, 290-291 (2017) 210-227.
[2] I. Brough, F.J. Humphreys, Evaluation and application of a fast EBSD detector, Materials Science and Technology, 26 (2010) 636-639.
[3] J. Guyon, N. Gey, D. Goran, S. Chalal, F. Pérez-Willard, Advancing FIB assisted 3D EBSD using a static sample setup, Ultramicroscopy, 161 (2016) 161-167.
[4] D. Wallis, L.N. Hansen, T. Ben Britton, A.J. Wilkinson, Geometrically necessary dislocation densities in olivine obtained using high-angular resolution electron backscatter diffraction, Ultramicroscopy, 168 (2016) 34-45.
[5] A.J. Wilkinson, G. Moldovan, T.B. Britton, A. Bewick, R. Clough, A.I. Kirkland, Direct Detection of Electron Backscatter Diffraction Patterns, Physical Review Letters, 111 (2013) 065506.
[6] A.A. Gazder, K.I. Elkhodary, M.J.B. Nancarrow, A.A. Saleh, Transmission Kikuchi diffraction versus electron back-scattering diffraction: A case study on an electron transparent cross-section of TWIP steel, Micron, 103 (2017) 53-63.
[7] E. Brodu, E. Bouzy, J.-J. Fundenberger, J. Guyon, A. Guitton, Y. Zhang, On-axis TKD for orientation mapping of nanocrystalline materials in SEM, Materials Characterization, 130 (2017) 92-96.
[8] C. Langlois, T. Douillard, H. Yuan, N. Blanchard, A. Descamps-Mandine, B. Van de Moortèle, C. Rigotti, T. Epicier, Crystal orientation mapping via ion channeling: An alternative to EBSD, Ultramicroscopy, 157 (2015) 65-72.

[9] D. Rowenhorst, A. Rollett, G. Rohrer, M. Groeber, M. Jackson, P.J. Konijnenberg, M. De Graef, Consistent representations of and conversions between 3D rotations, Modelling and Simulation in Materials Science and Engineering, 23 (2015) 083501.
[10] L. Giannuzzi, J. Michael, Comparison of channeling contrast between ion and electron images, Microscopy and Microanalysis, 19 (2013) 344-349.
[11] J.C. Slater, Atomic Radii in Crystals, The Journal of Chemical Physics, 41 (1964) 3199-3204.
[12] R.D. Shannon, C.T. Prewitt, Effective ionic radii in oxides and fluorides, Acta Crystallographica Section B, 25 (1969) 925-946.
[13] S. Vernier, J.-M. Franchet, M. Lesne, T. Douillard, J. Silvent, C. Langlois, N. Bozzolo, iCHORD-SI combination as an alternative to EDS-EBSD coupling for the characterization of γ-γ' nickel-based superalloy microstructures, Materials Characterization, 142 (2018) 492-503.
[14] G. Nolze, Image distortions in SEM and their influences on EBSD measurements, Ultramicroscopy, 107 (2007) 172-183.
[15] M.M. Nowell, S.I. Wright, Orientation effects on indexing of electron backscatter diffraction patterns, Ultramicroscopy, 103 (2005) 41-58.
[16] A. Morawiec, Orientations and rotations, Springer, 2003.
[17] G. Nolze, Euler angles and crystal symmetry, Crystal Research and Technology, 50 (2015) 188-201.
[18] P. Neumann, Representation of orientations of symmetrical objects by Rodrigues vectors, Textures and Microstructures, 14 (1991) 53-58.
[19] S. Singh, M.D. Graef, Orientation sampling for dictionary-based diffraction pattern indexing methods, Modelling and Simulation in Materials Science and Engineering, 24 (2016) 085013.
[20] A. Yershova, S. Jain, S.M. LaValle, J.C. Mitchell, Generating Uniform Incremental Grids on SO(3) Using the Hopf Fibration, The International journal of robotics research, 29 (2010) 801-812.
[21] Y.H. Chen, S.U. Park, D. Wei, G. Newstadt, M.A. Jackson, J.P. Simmons, M. De Graef, A.O. Hero, A dictionary approach to electron backscatter diffraction indexing, Microscopy and Microanalysis, 21 (2015) 739-752.